Multipole method for microstructured optical fibers. II. Implementation and results

Boris T. Kuhlmey

Institut Fresnel (Unité Mixte de Recherche du Centre National de la Recherche Scientifique 6133), Faculté des Sciences et Techniques de Saint Jérôme, 13397 Marseille Cedex 20, France, and School of Physics, University of Sydney, Sydney, New South Wales 2006, Australia

Thomas P. White

School of Physics, University of Sydney, Sydney, New South Wales 2006, Australia

Gilles Renversez and Daniel Maystre

Institut Fresnel (Unité Mixte de Recherche du Centre National de la Recherche Scientifique 6133), Faculté des Sciences et Techniques de Saint Jérôme, 13397 Marseille Cedex 20, France

Lindsay C. Botten

School of Mathematical Sciences, University of Technology, Sydney, New South Wales 2008, Australia

C. Martijn de Sterke

School of Physics, University of Sydney, Sydney, New South Wales 2006, Australia

Ross C. McPhedran

School of Physics, University of Sydney, Sydney, New South Wales 2006, Australia

Received October 4, 2001; revised manuscript received May 7, 2002

We describe the numerical verifications of a multipole formulation for calculating the electromagnetic properties of the modes that propagate in microstructured optical fibers. We illustrate the application of this formulation to calculating both the real and the imaginary parts of the propagation constant. We compare its predictions with the results of recent measurements of a low-loss microstructured fiber and investigate the variations in fiber dispersion with geometrical parameters. We also show that the formulation obeys appropriate symmetry rules and that these rules may be used to improve computational speed. © 2002 Optical Society of America

OCIS codes: 060.2280, 060.2400, 060.4510.

1. INTRODUCTION

In a previous paper, hereafter referred to as Part I,[1] we described the development of a multipole formulation for calculating the propagation and field characteristics of microstructured optical fibers (MOFs). Here we discuss numerical aspects of the formulation, the choice of its parameters to guarantee accurate results, and its numerical verification. The last is achieved through internal consistency tests and through a comparison both with other methods[2] and with recent experimental results obtained with a low-loss MOF structure.[3] We also present numerical results that illustrate important features of MOFs, such as the variation of the geometric loss of the modes that propagate in them and of their dispersion characteristics with MOF parameters. The numerical results given here and in Part I illustrate some key features of the formulation: incorporation of mode symmetry to answer definitively questions related to modal degeneracy, accurate and sensitive characterization of the geometric loss of modes, ability to deliver other modal data such as dispersion and field profiles, and modest computational requirements.

The description of numerical strategies here is of necessity detailed, because the location of modes requires the finding of an approximate zero of the determinant of a large complex matrix. Such zeros are often difficult to distinguish at first sight from false minima, and it is necessary to employ various validation criteria for the modes that correspond to the various putative zeros to identify physically meaningful solutions. It is of course valuable to have numerical or experimental values for similar systems to guide the mode search, and the curves and tables that we provide here and in Part I should provide a comprehensive aid to workers in the future.

0740-3224/2002/102331-10$15.00

2. VALIDATION AND SELF-CONSISTENCY

The formulation presented in Part I requires the finding of modes to satisfy a homogeneous equation or field identity of the form

$$[\mathbf{I} - \mathcal{R}(\tilde{\mathcal{H}} + \tilde{\mathcal{J}}^{B0}\tilde{\mathcal{R}}^{0}\tilde{\mathcal{J}}^{0B})]\mathcal{B} \equiv \mathcal{M}\mathcal{B} = 0. \quad (1)$$

This identity expresses the equality of two sets of field representations: a local expansion in the neighborhood of each cylindrical inclusion in the MOF,

$$E_z = \sum_{m=-M}^{M} [A_m^{El} J_m(k_\perp^e r_l) + B_m^{El} H_m^{(1)}(k_\perp^e r_l)]\exp(im\theta_l), \quad (2)$$

and a global, or Wijngaard, expansion,

$$E_z = \sum_{l=1}^{N_c} \sum_{m} B_m^{El} H_m^{(1)}(k_\perp^e |\mathbf{r}_l|)\exp[im \arg(\mathbf{r} - \mathbf{c}_l)] + \sum_{m} A_m^{E0} J_m(k_\perp^e r)\exp(im\theta). \quad (3)$$

The Wijngaard expansion is expressed in local coordinates by use of Graf's addition theorem, truncated to the chosen multipole order M and equated with local expansion (2). The two expansions for E_z and the corresponding expansions for the scaled magnetic-field component K_z match perfectly only for untruncated fields ($M \to \infty$), so their numerical difference on cylinder surfaces can be used as a powerful indicator of truncation errors and of the quality of the matrix null vector location. We illustrate this with an example, shown in Figs. 1 and 2, of an air-core MOF. Figure 1 shows significant field errors occurring near the boundary of the larger central air hole. As well, the low-frequency modulation of the field discrepancies indicates some imprecision in the minimization of the determinant. In Fig. 2 the multipole truncation order on the central hole has been increased to $M = 19$, whereas the truncation order on the smaller holes has been kept at 5. The decrease in field matching errors is evident (note the change in scale in between the bottom panels of Fig. 1 and those of Fig. 2) as is a slight improvement in the quality of the determinant minimization, manifested as a reduction in the low-frequency modulation. One clear sign of adequate convergence in the formulation is obtained from these comparison plots. When enough terms are included, the error term oscillates like the first neglected term in field expansions {i.e., like $\exp[i(M+1)\theta]$}.

A second test of convergence is of course provided by the stability of n_{eff} with respect to increase of M, as is illustrated in Table 1, where we also introduce

$$W = \frac{\int_{C_1} |E_z^{\text{local}}(\theta_1) - E_z^{\text{Wijngaard}}(\theta_1)| d\theta_1}{\int_{C_1} |E_z^{\text{Wijngaard}}(\theta_1)| d\theta_1}. \quad (4)$$

W is a measure of the accuracy of the equality between the local [Eq. (2)] and the Wijngaard [Eq. (3)] expansions. With increasing M, W decreases and n_{eff} stabilizes, as expected.

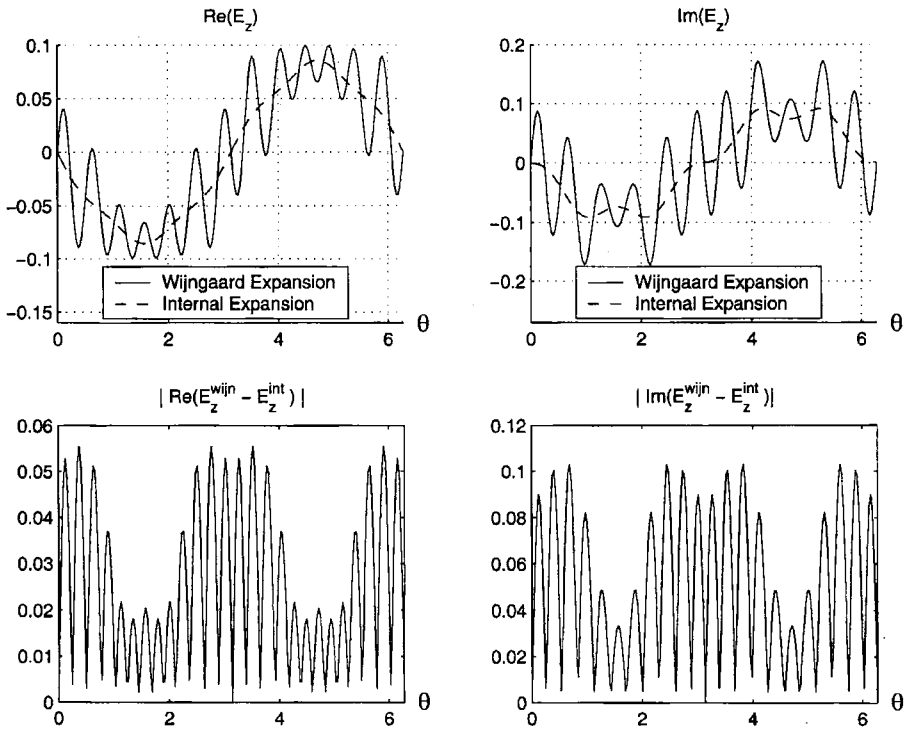

Fig. 1. Top, internal and bottom, Wijngaard expansions compared for $\Re(E_z)$ and $\Im(E_z)$, respectively, for an air core MOF, with $M = 5$ for both the central air hole and all other air holes (3 rings; 54 air holes of diameter 4.0271 μm; core hole diameter, 13.0714 μm; jacket diameter, 50 μm; $n_e = 1.39$; $n_i = 1.00$; $n_0 = 1.39 + 10^{-8}i$; $\Lambda = 5.78157$ μm; $\lambda = 3.846$ μm).

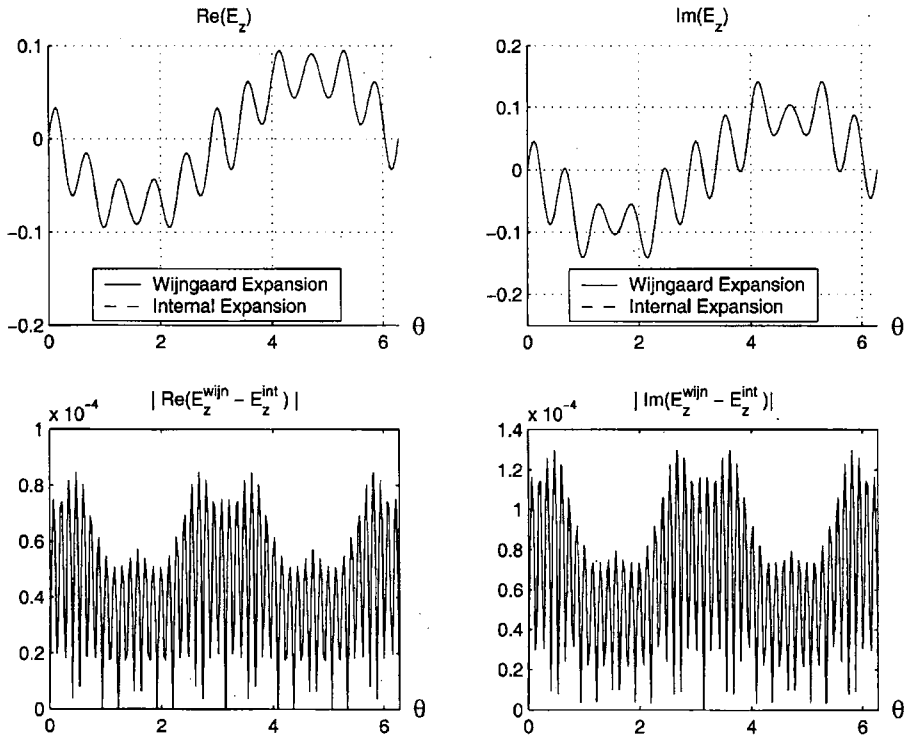

Fig. 2. As for Fig. 1 but with $M = 19$ for the core hole and $M = 5$ for all other holes. Note that the Wijngaard and internal expansions now match with graphic accuracy.

Table 1. Convergence of n_{eff} with M^a

M	$\Re(n_{\text{eff}})$	$\Im(n_{\text{eff}}) \times 10^6$	W
3	1.43852886240663	6.918242988502046	9.7×10^{-2}
4	1.43838719374803	1.749096334333127	4.6×10^{-2}
5	1.43836672605884	1.373925319699950	1.5×10^{-2}
6	1.43836499998690	1.414928166193201	2.7×10^{-3}
7	1.43836493475660	1.416468499483090	9.3×10^{-4}
8	1.43836493461317	1.416459892560528	7.7×10^{-4}
9	1.43836493424529	1.416475747100788	2.5×10^{-4}

[a] Results are for the $p = 1$ mode of the MOF in Table 1 of Part I at $\lambda = 1.45$ μm. Here W from Eq. (4) gives the degree of accuracy of the equality between Wijngaard and local expansions. The integrals are taken over the boundary of cylinder 1 situated at $r = 6.75$ μm, $\theta = 0$.

We have found that the choice of truncation parameter M should be made such that this quantity clearly exceeds (by a factor of $\sim$1.5) the largest argument of Bessel functions on the boundary of inclusions. This choice of M guarantees that the cylindrical functions of largest order in field expansions behave as cylindrical multipoles of electrostatics to leading order [i.e., as $r^n \exp(im\theta)$ and $r^{-n} \exp(im\theta)$] and ensures rapid convergence with increasing m. This criterion is manifest in Figs. 1 and 2, where many more Bessel terms are necessary for the large central hole than for other, smaller holes.

A powerful way to validate a new formulation is to compare its results with those of a well-established method. A comparison has already been made[2] of the results of our method with those of the scalar and vector beam propagation methods, for a MOF fiber that has a single ring of inclusions, and with the imaginary part of $n_{\text{eff}} = \beta/k_0$ of order 10^{-5}. We note that we have successfully used our formulation to study the effects of increasing the number of rings of inclusions, pushing the imaginary part of n_{eff} down to $\sim 10^{-11}$ by direct means before losing accuracy in its determination. In Section 5 we discuss an indirect method, which is capable of reaching lower values of the imaginary part.

As we also included in our software the extension of the present formalism to simulate the diffraction of incident light by the structure, we were able to validate the code thoroughly against results from other, well-established diffraction codes. Comparisons with a fictitious source code[4] and with other multipolelike codes[5,6] in conical incidence with complex or real permittivities in various geometries gave excellent agreement, to at least eight decimal places, for the radar cross section, validating each part of the code separately as well as in its entirety.

3. SYMMETRY

The incorporation of field symmetry into the multipole formulation has two benefits: First, it enables definitive statements to be made about the degeneracy of modes, even in the presence of the accidental degeneracies that arise when normally distinct modal trajectories cross each other. Second, it greatly reduces computational burdens, enabling accurate answers for quite large MOF structures to be obtained rapidly on personal computers (PCs).

In applying the multipole formulation to large sixfold symmetric MOFs it is highly advantageous to exploit the

symmetry properties in Fig. 3 of Part I to reduce the size of matrix $\mathcal{M}$. This can be achieved because only multipole coefficients for inclusions lying in the minimum sector indicated in Fig. 3 of Part I need be specified; those for holes outside the minimum sector can be obtained by multiplying by the appropriate geometric phase factor [related to $\exp(2\pi i/6)$]. The resultant reduction in the order of matrix $\mathcal{M}$ depends on the type of mode that is addressed; it is maximal for the nondegenerate modes in Fig. 3 of Part I and is ~3.5 for degenerate modes, leading to considerable reductions in processing time. See Appendix A for further details.

4. IMPLEMENTATION

Here we discuss the implementation of our method to find modes and dispersion characteristics of a given fiber structure.

A. Finding Modes

For the task of finding modes we need an algorithm aimed at finding all the zeros of the determinant of $\mathcal{M}$ in a region of the complex n_{eff} plane. The algorithm should be economical in function calls, as each evaluation of the determinant is computationally expensive for large structures. As shown in Fig. 2 of Part I, the zeros are sharp, so a highly accurate first estimate of the zero is necessary for most simple root-finding routines. More-specific algorithms for finding zeros of analytic or meromorphic functions[7,8] have good convergence for simple structures (with six cylinders, for example) but fail for more-complex structures, even with good initial guesses. Our present approach to root finding seems computationally efficient. We first compute a map of the modulus of the determinant over the region of interest and then use the local minima of this map as initial points for a mixed zooming and modified Broyden[9] algorithm (an iterative minimization algorithm, guaranteed to converge for parabolic minima). Further details of this method are given in Appendix B.

The initial scanning region has to be chosen in accordance with the physical problem studied: If the fiber is air cored, and air guided modes are sought, we choose $\Re(n_{\text{eff}}) < 1$, whereas if the fiber has a solid core we usually choose to search for modes in a region where $\Re(n_{\text{eff}})$ lies between the optical indices of the inclusions and the matrix. In the latter case hundreds of modes may exist for small $\Re(n_{\text{eff}})$, which are of little interest because of their high losses. We therefore often concentrate on a smaller n_{eff} scanning region near the highest index of the structure. A scanning region for $\Im(n_{\text{eff}})$ that gives good results in almost any case is $10^{-12} < \Im(n_{\text{eff}}) < 10^{-3}$.

B. Dispersion Characteristics

The process of finding modes as described above is carried out for a specific wavelength. We could repeat the search for modes for many different wavelengths to obtain dispersion characteristics, but this process would be quite laborious. We have found two other methods to be of value. One computes and identifies the modes for three or four different wavelengths, then uses a spline interpolation to estimate the n_{eff} values for other wavelengths, and refines the estimate with the mixed zooming and Broyden algorithm. Each newly determined point of the $n_{\text{eff}}(\lambda)$ curve can be used to enhance the spline estimate. The second (and often more efficient) method is to compute the modes for only one wavelength, λ_0, then slightly perturb the wavelength to get $n_{\text{eff}}(\lambda_0 + \delta_\lambda)$, with $n_{\text{eff}}(\lambda_0)$ used as a first guess, and then use a first-order estimate of n_{eff} at the next wavelength. One can then compute $n_{\text{eff}}(\lambda + m\delta_\lambda)$, using a first-order estimate computed from the two preceding values. For both methods the wavelength step has to be chosen very small: For small steps more points are necessary for computing the dispersion characteristics in a given wavelength range, but for large steps the first-order guess becomes inaccurate and the convergence of the zooming and Broyden algorithm unacceptably slow. Having small steps and therefore numerous numerical values on the dispersion curve is also of benefit when one is evaluating second-order derivatives, as is necessary to compute the group-velocity dispersion.

One can include material dispersion easily by changing the optical indices according to the current wavelength at each step, using, for example, a Sellmeier approximation[10] for silica.

The method described here can be adapted to a study of the change of n_{eff} of a mode for any continuously varying parameter, for example, cylinder radius, cylinder spacing, and optical index. One problem that can occur when one is following the evolution of a mode with a continuously varying parameter is mode crossing. Mode crossing results in wrong data but can easily be detected in most cases through a discontinuity of derivatives and can also easily be eliminated by restarting of the algorithm with the correct mode on the other side of the crossing.

The correct choice for δ_λ strongly depends on wavelength and structure, so no general advice can be given. However, as a rough guide, satisfactory results have generally required ~1000 points per unit λ/Λ on curves.

C. Using the Symmetry Simplifications

When the structure of interest presents symmetries, these can be used as described in Ref. 11 to improve the computations considerably, as mentioned in Subsection 3.B of Part I and detailed in Appendix A. The search for modes changes slightly in this case.

To obtain all the modes we now have to check for each class of mode separately. This entails going through the entire process of evaluating a determinant map and refining each local minimum once per nondegenerate mode class and once for each degenerate pair of mode classes. For a structure with C_{6v} symmetry, six determinant maps have to be evaluated [classes 1–3, 5, 7 and 8; the modes of classes 4 and 6 are deduced from those of classes 3 and 5 (cf. Fig. 3 of Part I)]. But, as the matrix size is reduced by a factor ranging from 3.5 to more than 6, and the computations scale as the size of the matrix cubed, the overall efficiency gain of using the symmetries remains high. The gain is even higher when dispersion figures are computed for a given mode, as only one symmetry class is then concerned.

D. Software and Computational Demands

We have developed a FORTRAN 90 code to exploit the considerations detailed above. For symmetric structures the

suggested optimizations are used and the software can therefore deal, even on PCs, with large structures (modes for fibers with 180 holes have so far been computed on current PCs). Once the structure has been defined, the software is able to find automatically all the modes within a given region of the complex plane for n_{eff} and can optionally track a mode as a function of wavelength to obtain dispersion characteristics. Material dispersion can be included, if desired.

Computational demands are relatively modest: The complete set of modes with $M = 5$ in the region of interest, $1.4 < \Re(n_{\mathrm{eff}}) < 1.45$ for the structure used in Figs. 2 and 4–6 of Part I, can be computed on a Pentium III (733-MHz) PC in less than 3 min, using less than 2 Mb of memory. Of course the load rises for larger structures, but the complete set of modes for a structure of three layers of holes in a hexagonal arrangement as used in Subsection 5.B of this paper takes less than 1 h (and ~15 Mb of memory) on a Compaq workstation. Dispersion curves can be computationally more expensive: The loss curves in Subsection 5.B took ~0.5 h (for $d/\Lambda = 0.075$, where we used $M = 5$) to several hours (for $d/\Lambda = 0.7$, where $M = 7$ was needed for accuracy).

5. FIBER GEOMETRY AND MODE PROPERTIES

A. Dispersion in Microstructured Optical Fibers

One of the important features of MOFs is the powerful control that their geometry exerts over the dispersion characteristics of modes.[12] In a standard single-mode fiber, the total dispersion consists of material and waveguide contributions, whose combination is normal in the near infrared for wavelengths up to $\lambda_{zc} \simeq 1.31\ \mu$m and is anomalous beyond that.[10] Dispersion-shifted fibers can shift the zero-dispersion point to longer wavelengths, whereas dispersion can be reduced over a range of wavelengths by other designs.

In Fig. 3 we show the evolution of key dispersion parameters with both wavelength and hole radius for a solid-core MOF with three rings of holes, for which the index of silica is modeled by the Sellmeier equation. The parameters displayed are $\Re(n_{\mathrm{eff}})$, $\Im(n_{\mathrm{eff}})$, v_g/c, and D, where

$$v_g = c\left(n_{\mathrm{eff}} + \omega\frac{\mathrm{d}n_{\mathrm{eff}}}{\mathrm{d}\omega}\right)^{-1} \tag{5}$$

is the group velocity[10] and

$$D = -\frac{\lambda}{c}\frac{\mathrm{d}^2\Re(n_{\mathrm{eff}})}{\mathrm{d}\lambda^2} \tag{6}$$

is the dispersion parameter. Noticeable trends in the four quantities are the steady decrease in $\Re(n_{\mathrm{eff}})$ as the hole size increases, the decrease in the loss or $\Im(n_{\mathrm{eff}})$ with increasing hole size and better confinement; the steady increase in group velocity with increasing air fraction; and the movement of λ_{zc} with hole diameter, initially above the step-index fiber value and then back down through it and sweeping toward the visible as d/Λ increases further. This ability to vary the zero-dispersion point by a wavelength factor that approaches 2 offers exciting possibilities for fiber designs.[12]

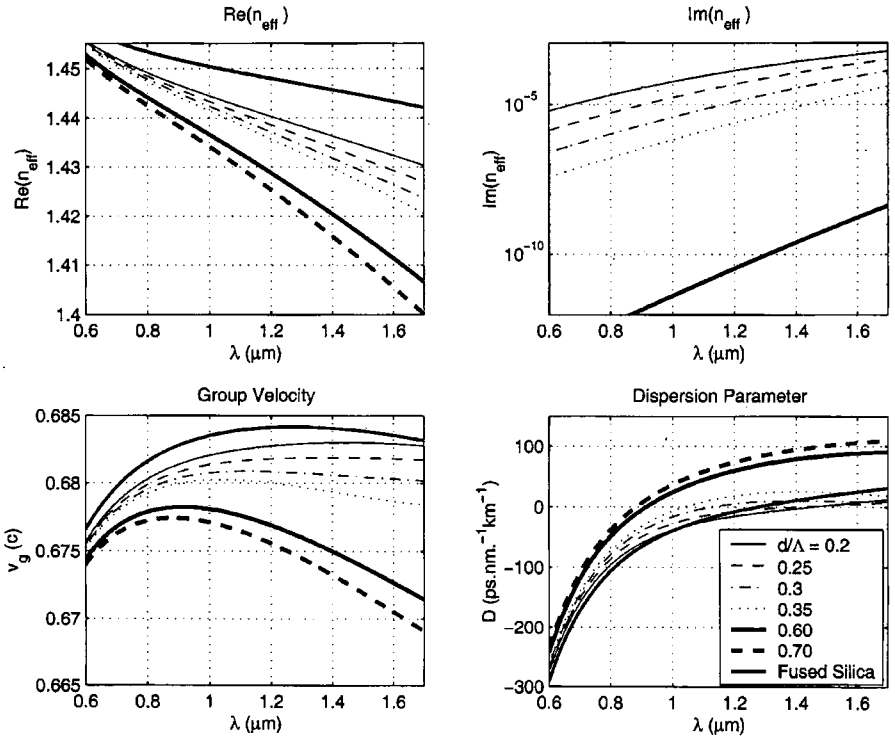

Fig. 3. Dispersion as a function of wavelength for solid-core MOFs in silica with three rings of holes for various values of d/Λ, with $\Lambda = 2.3\ \mu$m, $n_0 = n_{\mathrm{silica}}$, and the Sellmeier model for dispersion of silica.

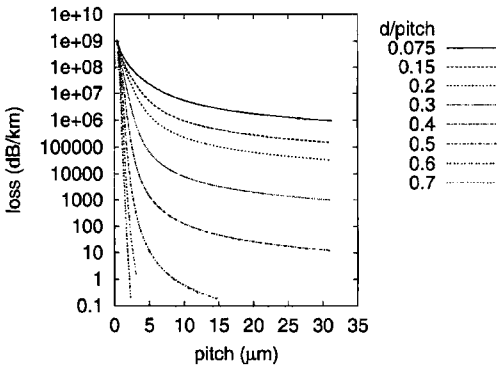

Fig. 4. Confinement loss figures for the fundamental mode of a MOF with three rings of air holes of various diameters and pitches. All curves are for $\lambda = 1.55\ \mu m$.

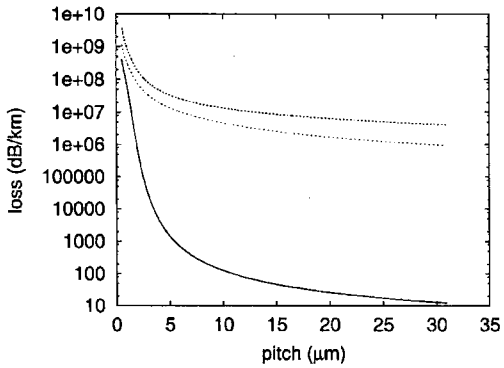

Fig. 5. Confinement loss figures for the first three modes of a MOF with three rings of air holes as a function of pitch. Here $d/\Lambda = 0.4$, $\lambda = 1.55\ \mu m$.

B. Confinement Losses

As modes in MOFs are not strictly confined but lossy, it is important to be able to evaluate the confinement losses that are intrinsically related to the MOF geometry. We studied the case of a silica MOF perforated with cylindrical air holes whose centers are arranged hexagonally and computed the loss figures for the first few modes at a wavelength of 1.55 μm, varying pitch, diameter-to-pitch ratio, and number of rings. In this study the jacket was taken to be made from silica.

Figure 4 shows the loss values for the fundamental mode of a solid-core MOF with three rings of holes with various pitches for different diameter-to-pitch ratios. It is clear that guidance becomes better for bigger holes, and our simulations show that larger pitches are favorable for lower losses. This can be explained phenomenologically as follows: The real part of the effective index of the fundamental mode tends to the refractive index of silica, so the propagation becomes increasingly parallel to the fiber axis. Interaction with the confining structure is thus minimized.

This behavior is also found for nonfundamental modes. Figure 5 shows the loss values with various pitches for the first three modes of a MOF with three rings of holes, for a diameter-to-pitch ratio of $d/\Lambda = 0.4$. Note that nonfundamental modes always exist, even for structures claimed to be single mode, but can be much more lossy than the fundamental mode. As losses vary continually with parameters and no truly bound modes exist in the case of MOFs, the definition of a single-mode MOF can be only relative. Moreover, it emerges from our numerical results that introducing an air jacket about the MOF makes these three modes truly bound [$\Im(n_{\text{eff}}) = 0$], while others remain leaky. This phenomenon shows the importance of the jacket and is currently under investigation.

Data showing confinement loss as a function of the number of rings and their diameter-to-pitch ratio, with $\Lambda = 2.3\ \mu m$, for a wavelength $\lambda = 1.55\ \mu m$, have already been reported.[13] Depending on the value of d/Λ, as many as eight rings of holes were necessary to reduce confinement loss below 1 dB/m.

6. THEORY AND EXPERIMENT

We compared results from our simulations with experimental data published by Kubota *et al.*[3] The MOF used for their experiments was a silica fiber with approximately seven rings of air holes disposed in a regular hexagonal lattice whose core is created by a missing hole (Fig. 6). For our simulations we used the geometrical data as published but varied the number of rings from one to seven. We used the Sellmeier approximation for the index of silica.

A first result is that there is no need to have a large number of rings to reach confinement losses of the order of losses of conventional fibers. Figure 7 shows the loss figures for the first three modes versus the number of rings at a wavelength of 0.76 μm. These figures include only confinement losses, not absorption or Rayleigh scattering; they show the limitations that are due to the confinement by a MOF structure.

With two rings, the fiber exhibits single-mode behavior for kilometric lengths, as only the fundamental mode propagates without significant losses, but with more than two rings other modes become virtually lossless. This result is in agreement with the multimode behavior observed experimentally for seven rings of holes. Clearly, three rings of holes are theoretically enough to ensure

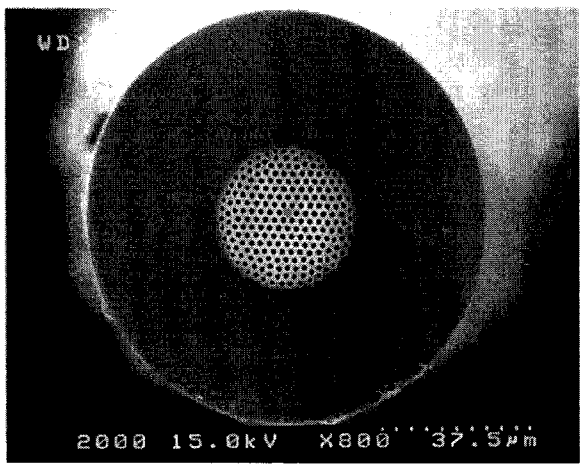

Fig. 6. Scanning-electron micrograph of a cleaved end face of the MOF fabricated by Kubota *et al.*[3] used in our comparisons. Figure supplied by H. Kubota.

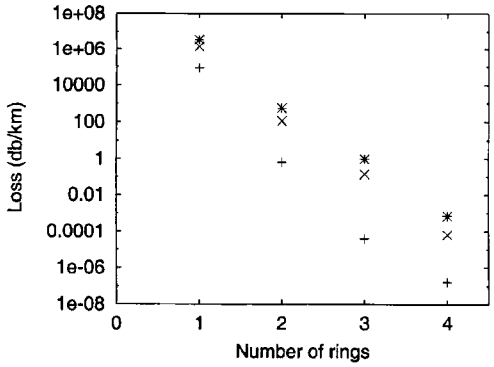

Fig. 7. Loss of the first three modes as a function of number of rings for the structure published by Kubota *et al.*,[3] at a wavelength of 0.76 μm. Only confinement losses are included.

guidance that is limited only by losses caused by absorption or structural imperfections. We confirm that the losses observed by Kubota *et al.* (7.1 dB/km at 850 nm) are due not to the limitation imposed by the MOF geometry of the fiber but mainly to Rayleigh scattering, structural imperfections, or absorption.

The imaginary parts of n_{eff} that correspond to Fig. 7 are well below those that can be determined directly by determinant minimization. Instead we must proceed through the evaluation of $\Im(n_{\text{eff}})$ by an energy flux argument, once the real part of n_{eff} has been determined to high accuracy by determinant minimization. Loss coefficient α is obtained through the conservation of the time-averaged flux of Poynting vector $\mathbf{S}$ through a cylinder of elementary length δz centered at the origin and with a radius R such that the cylinder includes all inclusions. We have

$$\int\int_{\theta,\rho<R} \Re[\mathbf{S}(\rho,\ \theta,\ z)] \cdot \hat{u}_z \rho \mathrm{d}\rho \mathrm{d}\theta = \delta z \oint_\theta \Re[\mathbf{S}(R,\ \theta,\ z)] \cdot \hat{u}_r R \mathrm{d}\theta + \int\int_{\theta,\rho<R} \Re[\mathbf{S}(\rho,\ \theta,\ z+\delta z)] \cdot \hat{u}_z \rho \mathrm{d}\rho \mathrm{d}\theta, \quad (7)$$

where $\hat{u}_z$ and $\hat{u}_r$ are the usual unit vectors of the local basis in cylindrical coordinates. As $\mathbf{S}$ varies as $e^{-\alpha z}$, we have

$$\mathbf{S}(\rho,\ \theta,\ z+\delta z) \simeq (1-\alpha\delta z)\mathbf{S}(\rho,\ \theta,\ z), \quad (8)$$

so Eq. (7) becomes

$$\alpha \int\int_{\rho<R,\theta} \Re[\mathbf{S}(\rho,\ \theta,\ z)] \cdot \hat{u}_z \rho \mathrm{d}\rho \mathrm{d}\theta = \oint_\theta \Re[\mathbf{S}(R,\ \theta,\ z)] \cdot \hat{u}_r R \mathrm{d}\theta. \quad (9)$$

Isolating α gives

$$\alpha = \frac{\oint_\theta \Re[S_r(R,\ \theta,\ z)] R \mathrm{d}\theta}{\int\int_{\theta,\rho<R} \Re[S_z(\rho,\ \theta,\ z)] \rho \mathrm{d}\rho \mathrm{d}\theta}, \quad (10)$$

where we have introduced S_z and S_r, components of $\mathbf{S}$ in cylindrical coordinates. The imaginary part of the effective index is then given by

$$\Im(n_{\text{eff}}) = \frac{\alpha}{2k_0}. \quad (11)$$

We computed dispersion figures for the fundamental mode of the Kubota structure. We first observed that, for this structure, the number of rings has little influence on the actual dispersion curve, as the fundamental mode is already well confined with one ring. We therefore used a one-ring structure in subsequent simulations to improve computational speed without losing significant accuracy for dispersion parameters. Although we observed a shift of the zero-dispersion wavelength to the 800-nm band, we did not find exact agreement with the experimental zero-dispersion wavelength of 810 nm. With the given geometrical data we found a zero-dispersion wavelength of 889 nm. Kubota *et al.* found similar results with a finite-difference time-domain method. To explain the difference from experimental data we computed the zero-dispersion wavelength for various hole pitches and diameters: In Fig. 8, pitch is varied and diameter is held constant; in Fig. 9, diameter is varied and pitch is held constants; in Fig. 10, pitch and diameter are both varied

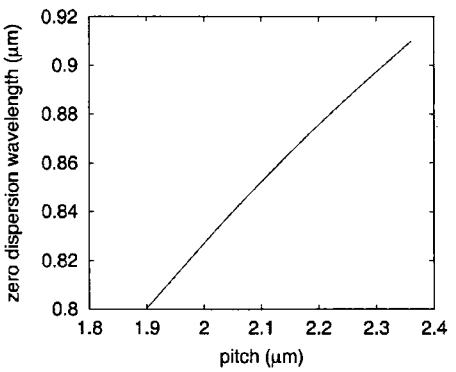

Fig. 8. Zero-dispersion wavelength as a function of pitch for the structure published by Kubota *et al.*,[3] with constant diameter $d = 1.51$ μm.

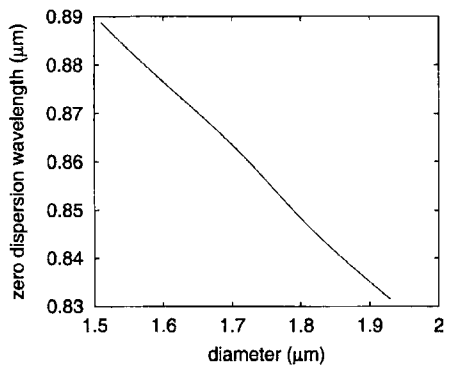

Fig. 9. Zero-dispersion wavelength as a function of hole diameter for the structure published by Kubota *et al.*,[3] with constant pitch $\Lambda = 2.26$ μm.

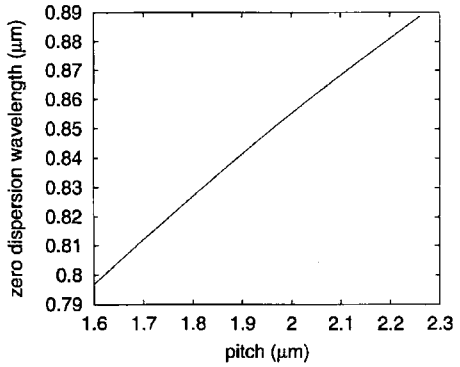

Fig. 10. Zero-dispersion wavelength as a function of pitch for the structure published by Kubota *et al.*,[3] with constant diameter/pitch ratio $d/\Lambda = 0.67$.

and the pitch/diameter ratio is held constant. These figures show that a variation of ~15% in pitch with a constant diameter or of 25% in pitch with a constant diameter/pitch ratio is necessary to produce the experimental zero dispersion wavelength.

7. CONCLUSIONS

The accuracy and computational speed of the multipole formulation described above offer important advantages for understanding or exploiting the properties of MOF fibers. The results presented show clearly the details of field structures and symmetry properties. The formulation is at present limited to designs composed of nonintersecting circular inclusions; nevertheless, it can be employed in studies ranging over a wide parameter space: hole radius, spacing, number of rings, packing geometry, air or solid core, etc. As we saw, the strong index contrast between air and silica means that fiber parameters can be tuned across a wide range as these parameters vary, so MOF fibers may well offer a new generation of fiber devices with novel properties. Multipole formulations will be a valuable tool in the quest to develop these devices.

One interesting issue that merits further investigation was raised in Section 5. The structure formulated by Kubota *et al.*[3] was shown to be single moded for two rings of air holes and multimoded for kilometric lengths with three or more rings. The identification of the number of modes that are physically significant at a particular wavelength depends on the fiber length in question, which dictates the upper limit on mode loss, which is one factor in deciding how many modes can compete to carry energy from one end of the fiber to the other. As we have seen, mode loss varies strongly with mode number, hole spacing and size, and number of rings of holes. Thus a comprehensive numerical study will be necessary to provide data on mode loss as a function of these parameters from which a useful definition of mode number in MOFs may emerge.

Finally, we add a few remarks that place our multipole method in the context of the range of competing techniques for numerically studying MOF's. First, as we have shown, the multipole method is capable of yielding the geometric loss of finite MOF confining structures, with $\Im(n_{\text{eff}})$ accessible to 10^{-14} or lower. This is a property that is not likely to be emulated easily by other methods and is certainly unique at this time. Second, the method has been constructed in such a way that symmetry properties of modes can be enforced within the formulation, so questions of degeneracy are exactly answered. Third, it delivers highly accurate data on propagation constants and field patterns for modes by using quite modest computing resources if the MOF contains a reasonable number of air holes. There are drawbacks to the method, of course: It is at present restricted to circular air holes, and mode searching for an unfamiliar geometry may be difficult and time consuming. Nevertheless, the multipole formulation is likely to prove highly valuable in coming years, as designers move to exploit the manifold possibilities afforded by a new generation of optical fibers.

APPENDIX A: SYMMETRIZATION OF MODES

We consider waveguides with C_{6v} symmetry, such as the structures in Fig. 6. As was shown by McIsaac,[14] such structures have eight mode classes, four of which occur as two degenerate pairs, as shown in Fig. 3 of Part I. For the purpose of this example we are interested in the degenerate fundamental modes $p = 3$ and $p = 4$ and in the lowest-order nondegenerate modes $p = 1$ and $p = 2$. The minimum waveguide segments illustrated in Fig. 3 of Part I represent the smallest segment of fiber required for fully defining the modal fields of the complete structure. We relate the multipole coefficients for a secondary cylinder outside the minimum segment to those of the corresponding primary cylinder inside the segment.

From Fig. 3 of Part I, nondegenerate mode classes 1 and 2 have minimum waveguide segments of $\pi/6$, so 3 primary cylinders are required for describing the 18-hole structure shown in Fig. 11. The holes are labeled P_S, where P is the primary cylinder and S is the label given to the secondary cylinder. Hole 1_1 is primary cylinder 1 and lies in the inner shell; the other primary cylinders, 2_1 and 3_1, lie in the second shell. As they are not degenerate, these modes must exhibit the full sixfold symmetry of the structure.

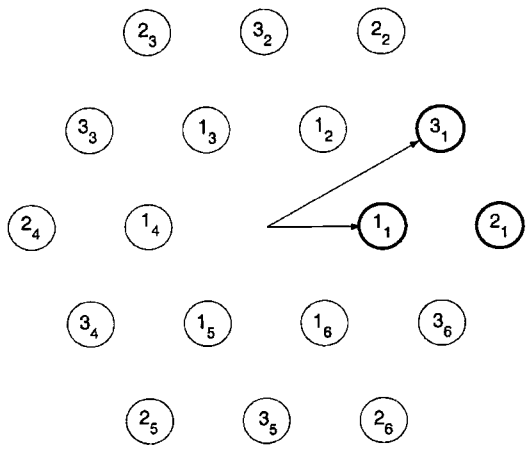

Fig. 11. Primary (bold circles) and secondary cylinders of the nondegenerate $p = 1$ and $p = 2$ mode classes of a two-ring MOF structure.

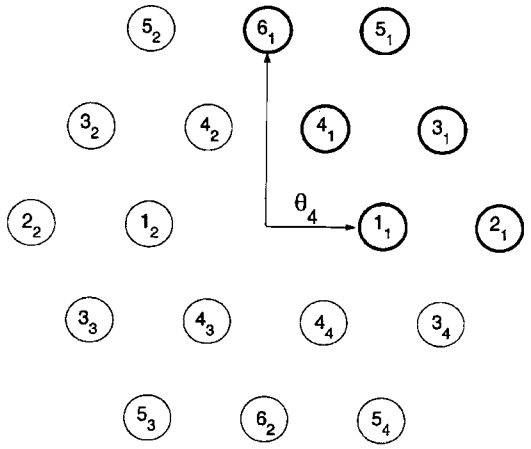

Fig. 12. Primary (bold circles) and secondary cylinders of the degenerate $p = 3$ and $p = 4$ mode classes of a two-ring MOF structure.

In terms of the multipole coefficients of the electric field b_m^E, the relation between those on secondary cylinders to those on primary cylinders can be expressed in the form

$$b_m^{E(P_S)} = b_m^{E(P_1)} \exp[im(S-1)\pi/3],$$

and similarly for the magnetic-field coefficients.

For degenerate mode classes 3 and 4, the number of secondary cylinders that correspond to a given primary cylinder depends on the position of the primary cylinder. If the primary cylinder lies on a symmetry axis of the mode, in this case either the x or the y axis, then only one other cylinder is related to it. A primary cylinder that is not on a symmetry axis has three associated secondary cylinders. A cylinder positioned at the center of the structure has no secondary cylinders. The related primary and secondary cylinders are shown in Fig. 12.

For classes 3 and 4 the fields are either symmetric or antisymmetric about the transverse axes. The relation between primary and secondary cylinders is obtained by appropriate combinations of reflections and inversions to give the correct symmetry properties.

For mode $p = 3$ the multipole coefficients on a secondary cylinder lying on the x axis are related to those on the corresponding primary cylinder by a simple reflection of E_z and antireflection of K_z across the y axis:

$$b_m^{E(P_2)} = -b_{-m}^{E(P_1)}, \qquad b_m^{K(P_2)} = b_{-m}^{K(P_1)}.$$

Similarly, for a secondary cylinder on the y axis the relations are

$$b_m^{E(P_2)} = (-1)^m b_{-m}^{E(P_1)}, \qquad b_m^{K(P_2)} = (-1)^{m+1} b_{-m}^{K(P_1)}.$$

As mentioned above, a primary cylinder that does not lie on either axis has three associated secondary cylinders. The relations are again combinations of reflections and antireflections about the axes:

$$b_m^{E(P_2)} = -b_{-m}^{E(P_1)}, \qquad b_m^{K(P_2)} = b_{-m}^{K(P_1)},$$

$$b_m^{E(P_3)} = (-1)^{m+1} b_m^{E(P_1)}, \qquad b_m^{K(P_3)} = (-1)^{m+1} b_m^{K(P_1)},$$

$$b_m^{E(P_4)} = (-1)^m b_{-m}^{E(P_1)}, \qquad b_m^{K(P_4)} = (-1)^{m+1} b_{-m}^{K(P_1)}.$$

We obtain the relations for the second degenerate mode class $p = 4$ simply by swapping the b_m^E and b_m^K coefficients in the equations above.

These symmetry relations are used in our method to reexpress field identity (1) in terms of the primary cylinders only. This reduces the matrix dimensions by a factor of 3.5–6, depending on the mode class, thus greatly increasing the calculation speed and allowing larger structures to be studied.

APPENDIX B: ALGORITHM

We compute the determinant for a number of points $0 \leq i_r \leq N_r$ over $0 \leq i_i \leq N_i$ lines parallel to the real axis, with imaginary parts varying exponentially with i_i. The exponential variation of the imaginary part is necessary, as different modes can have losses that differ by several orders of magnitude. Local minima of this array are computed through simple data analysis, and better initial guesses of the minima are estimated through interpolation of the points adjacent to each minimum. This guess is used as a starting point for a Broyden-like algorithm. If the algorithm fails, a new map of the determinant is computed over the region in which the first mapping showed that there is a local minimum. This refinement map uses a region of 5×5 points, with a linear scale for both real and imaginary parts. If the only minima of the refined region are on its border, the region is extended until a minimum lies inside the region. During the enlargement of the region, care is taken to prevent regions from overlapping regions in which computing errors can occur (negative or excessive imaginary or real part). If a minimum is found in the refined region (excluding the borders), the routine tries the Broyden-like algorithm again. If multiple minima are found in the region, each minimum is added to the initial minima list and is treated separately: Missing a zero thus becomes highly unlikely. During the Broyden algorithm a calculation of singular values is performed (see Subsection 3.A of Part I) each time the modulus of the determinant for the current point is less than a parameterized threshold, and we analyze the modules of the eigenvalues to determine whether an acceptable solution has been found (see the discussion in Subsection 3.A of Part I).

The routine continues to alternate Broyden and zooming algorithms until one of the following occurs:

- An acceptable solution is found,
- The extended mapping region concentrates near a border of the initial region,
- The refined region becomes too small,
- The extended mapping region includes a minimum of the initial determinant map that has already been treated, or
- A maximum number of iterations is reached.

Depending on the width of the initial scanning region and the complexity of the structure, the pertinent choice of N_r varies from ~50 to several hundreds: Structures with a substantial number of cylinders have a higher density of modes and therefore need a better resolution on the initial determinant map. The value of N_i, even for intricate structures, does not need to be high and is usu-

ally taken from 4 to 8. As shown in Fig. 2 of Part I, zeros are usually associated with valleys parallel to the imaginary axis, so precise maps parallel to the real axis for a few values of the imaginary part are sufficient for finding a first estimate of the zeros.

ACKNOWLEDGMENTS

This study was supported by the Australian Research Council. It has benefitted from travel support provided by the French and Australian governments. H. Kubota is thanked for discussion of experimental results and provision of figures.

R. C. McPhedran's e-mail address is ross @physics.usyd.edu.au.

REFERENCES

1. T. P. White, B. T. Kuhlmey, R. C. McPhedran, D. Maystre, G. Renversez, C. M. de Sterke, and L. C. Botten, "Multipole method for microstructured optical fibers. I. Formulation," J. Opt. Soc. Am. B **19**, 2322–2330 (2002).
2. M. J. Steel, T. P. White, C. M. de Sterke, R. C. McPhedran, and L. C. Botten, "Symmetry and degeneracy in microstructured optical fibers," Opt. Lett. **26**, 488–490 (2001).
3. H. Kubota, K. Suzuki, S. Kawanishi, M. Nakazawa, M. Tanaka, and M. Fujita, "Lowloss, 2-km-long photonic crystal fiber with zero GVD in the near IR suitable for picosecond pulse propagation at the 800 nm band," in *Conference on Lasers and Electro-Optics (CLEO2001)*, Vol. 56 of OSA Trends in Optics and Photonics Series (Optical Society of America, Washington, D.C., 2001), paper C3.
4. F. Zolla and R. Petit, "Method of fictious sources as applied to the electromagnetic diffraction of a plane wave by a grating in conical mounts," J. Opt. Soc. Am. A **13**, 1087–1096 (1996).
5. D. Felbacq, G. Tayeb, and D. Maystre, "Scattering by a random set of parallel cylinders," J. Opt. Soc. Am. A **11**, 2526–2538 (1994).
6. E. Centeno and D. Felbacq, "Rigorous vector diffraction of electromagnetic waves by bidimensional photonic crystals," J. Opt. Soc. Am. A **17**, 320–327 (2000).
7. P. Kravanja and M. Van Barel, *Computing the Zeros of Analytic Functions* (Springer-Verlag, Berlin, 2000).
8. L. C. Botten, M. S. Craig, and R. C. McPhedran, "Complex zeros of analytic functions," Comput. Phys. Commun. **29**, 245–259 (1983).
9. C. G. Broyden, "A class of methods for solving nonlinear simultaneous equations," Math. Comput. **19**, 577–593 (1965).
10. G. P. Agrawal, *Nonlinear Fiber Optics* (Academic, San Diego, Calif., 1995).
11. E. Yamashita, S. Ozeki, and K. Atsuki, "Modal analysis method for optical fibers with symmetrically distributed multiple cores," J. Lightwave Technol. **3**, 341–346 (1985).
12. D. Mogilevtsev, T. A. Birks, and P. St. J. Russell, "Group-velocity dispersion in photonic crystal fibers," Opt. Lett. **23**, 1662–1664 (1998).
13. T. P. White, R. C. McPhedran, C. M. de Sterke, and M. J. Steel, "Confinement losses in microstructured optical fibers," Opt. Lett. **26**, 488–490 (2001).
14. P. R. McIsaac, "Symmetry-induced modal characteristics of uniform waveguides. I. Summary of results," IEEE Trans. Microwave Theory Tech. **MTT-23**, 421–429 (1975).